

The temporal evolution of non-neutralized electric currents and the complexity of solar active regions

IOANNIS KONTOGIANNIS ¹ AND MANOLIS K. GEORGOULIS ^{2,3}

¹*Leibniz-Institut für Astrophysik Potsdam (AIP) An der Sternwarte 16, 14482 Potsdam, Germany*

²*Space Exploration Sector, Johns Hopkins Applied Physics Laboratory, Laurel, MD 20723, USA*

³*Research Center for Astronomy and Applied Mathematics of the Academy of Athens, 11527 Athens, Greece*

(Received ; Revised ; Accepted)

Submitted to ApJ

ABSTRACT

We study the evolution of electric currents during the emergence of magnetic flux in the solar photosphere and the differences exhibited between solar active regions of different Hale complexity classes. A sample of 59 active regions was analyzed using a method based on image segmentation and error analysis to determine the total amount of non-neutralized electric current along their magnetic polarity inversion lines. The time series of the total unsigned non-neutralized electric current, $I_{NN,tot}$, exhibit intricate structure in the form of distinct peaks and valleys. This information is largely missing in the respective time series of the total unsigned vertical electric current I_z . Active regions with δ -spots stand out, exhibiting 1.9 times higher flux emergence rate and 2.6 times higher $I_{NN,tot}$ increase. The median value of their peak $I_{NN,tot}$ is equal to $3.6 \cdot 10^{12}$ A, which is more than three times higher than that of the other regions of the sample. An automated detection algorithm was also developed to pinpoint the injection events of non-neutralized electric current. The injection rates and duration of these events were higher with increasing complexity of active regions, with regions containing δ -spots exhibiting the strongest and longest events. These events do not necessarily coincide with increasing magnetic flux, although they exhibit moderate correlation. We conclude that net electric currents are injected during flux emergence, but are also shaped drastically by the incurred photospheric evolution, as active regions grow and evolve.

Keywords: Delta sunspots, solar active regions magnetic fields, solar magnetic fields, solar active regions, magnetohydrodynamics, solar activity

1. INTRODUCTION

Active regions form when buoyant magnetic flux tubes rise from the interior of the Sun (van Driel-Gesztelyi & Green 2015), and appear in the photosphere, forming pores, sunspots and/or groups of sunspots (Zwaan 1985, 1987) of varying size and complexity. Their white light morphology and distribution of magnetic polarities can be used to categorize them in terms of magnetic complexity (Hale et al. 1919). Active regions can be as simple as isolated sunspots surrounded by plage regions (α -type), bipolar or multipolar sunspot groups

consisting of well-, or not so well-, separated polarities (β - and $\beta\gamma$ -type), and in some cases they include opposite-polarity umbrae sharing the same penumbra (δ -type regions, Künzel 1965). Different complexity categories can also reflect different evolutionary states, as active regions emerge and evolve (McIntosh 1990). Although most regions are relatively simple and classified as β (bipolar; Jaeggli & Norton 2016), the most complex active regions (δ -spots) exhibit sheared polarity inversion lines (PILs) characterized by exceptionally strong electric currents and are the ones most often associated with strong flares and coronal mass ejections (CMEs) (Sammis et al. 2000; Toriumi & Wang 2019).

The existence of strong electric currents owing to complex magnetic fields was noticed already several decades

ago (Severnyi 1965; Alfvén & Carlqvist 1967). Although concerns were raised against the realism and feasibility of calculation of these currents (Parker 1996; Wilkinson et al. 1992), when appropriate spectropolarimetric observations became commonplace, strong indications occurred that the inferred currents from Ampere’s law are reasonably realistic and reflect true physical characteristics (Leka et al. 1996; Semel & Skumanich 1998; Wheatland 2000; Georgoulis et al. 2012). These studies further showed that some active region electric currents exhibited non-neutrality, meaning that their photospheric magnetic footprints deviated from the archetypal isolated shielded flux tubes predicted by theory (Parker 1979) and discussed in studies of isolated magnetic elements (Venkatakrishnan & Tiwari 2009). A theoretical framework as well as merits and caveats of the study of electric currents in solar active regions can be found in Georgoulis (2018). In the nominal case of isolated flux tubes embedded in a field-free plasma, a volume (direct) electric current is shielded by an equal and oppositely directed (return) sheath current. This symmetry possibly breaks in cases of very close proximity of opposite-polarity footprints such as, prominently, intense magnetic polarity inversion lines. In such exceptional cases, electric currents are non-neutralized and raw currents are injected in the solar atmosphere, supplying the otherwise non-neutralized currents of the overwhelmingly space-filling coronal magnetic fields (Longcope & Welsch 2000).

Recent studies have showcased the importance of the electric currents in the context of the pre-eruption evolution of solar active regions (Georgoulis et al. 2019), as well as the three-dimensional standard flare model (Aulanier et al. 2012, 2013; Janvier et al. 2013, 2014). Overall, flaring active regions exhibit at least an order of magnitude higher non-neutralized electric currents than flare-quiet ones (Kontogiannis et al. 2017, 2018) and the same quantity is highly correlated with the kinematic characteristics of CMEs (Kontogiannis et al. 2019). Regions prone to eruptions are reported to exhibit a higher degree of non-neutralization (Liu et al. 2017; Vemareddy 2019; Avallone & Sun 2020; Liu et al. 2024). Localized, intense changes of the vertical electric current density have also been associated with pre-flaring activity and free energy build-up (Mitra et al. 2020; Sahu et al. 2023). Flux-ropes with non-neutralized electric currents at their footpoints may well be kink-unstable (Tsap et al. 2022), which seems to be corroborated by

at least some observed flaring active regions (Barczynski et al. 2020; Wang et al. 2023).

But what is the origin of non-neutralized electric currents in solar active regions? Simulations show that the development of non-neutralized electric currents is a consequence of flux emergence and the subsequent photospheric motions, which lead to the formation of PIL and strong magnetic shear (Török et al. 2014; Dalmasse et al. 2015). The coexistence of strong electric currents and PILs is substantiated by observational studies (see e.g., Kontogiannis et al. 2019; Kazachenko et al. 2022). On the other hand, Georgoulis et al. (2012) propose that the close interaction between opposite magnetic polarities leads to the breaking of cylindrical symmetry and the development of shear and strong electric currents through the Lorentz force. In the same study, the coherence found in the electric current carried by the magnetic polarities points to a sub-photospheric origin of electric currents. What is, then, the evolution of the electric current in active regions and what conclusions can be drawn from its scrutiny? This question is relevant to how some active regions eventually become so complex. Although several studies have focused on the evolution of the magnetic flux during flux emergence (Otsuji et al. 2011; Norton et al. 2017; Kutsenko et al. 2019), no study so far has been dedicated to the evolution of non-neutralized electric currents in a sizeable sample of emerging active regions. Smaller samples of regions/events have been scrutinized using the degree of current neutralization (e.g., Liu et al. 2017; Avallone & Sun 2020; He et al. 2020; Wang et al. 2023; Liu et al. 2024), whose calculation is based on assumptions regarding direct and return currents.

In the present study we examine a statistically significant sample of emerging active regions of different magnetic complexity (in terms of Hale class), following a methodology (Section 2) that calculates the non-neutralized electric current using morphological image processing and taking into account the systematic and numerical errors as in Georgoulis et al. (2012). In Section 3, we discuss a few case studies of specific active regions emphasizing the evolution of electric current in different complexity classes. We then present the characteristics of the non-neutralized electric currents time series in comparison to the time series of the magnetic flux and as a function of Hale class. Additionally, we analyze the time series in terms of injection events and their properties. In Section 4, we summarize and discuss the results in the context of the origin of electric currents in active regions and the formation of δ -spot regions.

Table 1. The sample of emerging active regions used in this study. The table contains information regarding their National Oceanic and Atmospheric Administration (NOAA) identifier, the start and end date of each HARP data set, the start and end heliographic longitude at which each region was observed, the resulting number of processed magnetograms (the number of points in the time series), the peak Hale class each region reached over the observation interval, and the number of flares associated with each region (see text).

Number	NOAA	Start Date	End Date	Start long. (Degrees)	End long. (Degrees)	Number of magnetograms	Hale class	Flare class
1	11440	19-Mar-2012 00:46	26-Mar-2012 19:10	-22.87	93.00	853	$\beta\gamma\delta$	4 C
2	11267	4-Aug-2011 10:10	12-Aug-2011 11:22	-46.62	58.76	963	$\beta\gamma\delta$	1 B, 4 C
3	11465	19-Apr-2012 14:46	30-Apr-2012 13:10	-57.92	90.97	1300	$\beta\gamma\delta$	3 B, 16 C
4	11640	29-Dec-2012 12:10	8-Jan-2013 10:46	-40.28	87.82	1191	$\beta\gamma\delta$	7 B, 7 C
5	11726	19-Apr-2013 04:22	27-Apr-2013 09:10	-19.41	88.68	924	$\beta\gamma\delta$	11 B, 56 C, 1 M
6	11158	10-Feb-2011 21:58	21-Feb-2011 07:34	-40.26	92.56	1247	$\beta\gamma\delta$	1 B, 56 C, 5 M, 1 X
7	11750	15-May-2013 00:58	21-May-2013 18:58	0.4265	90.19	808	$\beta\gamma\delta$	6 C
8	12673	28-Aug-2017 08:58	10-Sep-2017 11:10	-81.77	89.12	1431	$\beta\gamma\delta$	1 B, 54 C, 26 M, 4 X
9	11515	26-Jun-2012 03:58	10-Jul-2012 03:10	-81.46	88.61	1668	$\beta\gamma\delta$	2 B, 73 C, 30 M, 1 X
10	11884	26-Oct-2013 06:58	8-Nov-2013 10:46	-83.82	88.84	1571	$\beta\gamma\delta$	1 B, 15 C, 4 M
11	12257	4-Jan-2015 03:46	14-Jan-2015 14:46	-50.51	89.60	1252	$\beta\gamma\delta$	23 C, 3 M
12	11561	30-Aug-2012 00:22	5-Sep-2012 20:10	-29.26	62.02	727	$\beta\gamma\delta$	
13	11645	2-Jan-2013 19:34	8-Jan-2013 23:10	-12.42	75.48	736	$\beta\gamma\delta$	2 C
14	11431	4-Mar-2012 11:10	10-Mar-2012 09:22	14.617	94.20	681	$\beta\gamma\delta$	
15	11273	16-Aug-2011 13:10	21-Aug-2011 16:34	-18.69	52.27	618	$\beta\gamma\delta$	
16	11179	21-Mar-2011 09:58	26-Mar-2011 22:22	-16.62	61.42	606	$\beta\gamma$	
17	11327	18-Oct-2011 23:58	28-Oct-2011 16:34	-38.71	87.77	1107	$\beta\gamma$	
18	11813	6-Aug-2013 14:10	12-Aug-2013 11:34	-13.30	69.01	699	$\beta\gamma$	1 B
19	11776	18-Jun-2013 11:34	26-Jun-2013 00:58	-11.47	90.45	907	$\beta\gamma$	5 B, 5 C
20	11824	17-Aug-2013 06:10	22-Aug-2013 07:10	2.1014	75.38	597	$\beta\gamma$	1 C
21	11922	10-Dec-2013 00:22	15-Dec-2013 19:22	4.4104	89.78	696	$\beta\gamma$	
22	12353	19-May-2015 11:10	27-May-2015 22:10	-46.09	74.15	1008	$\beta\gamma$	1 B, 3 C
23	11416	8-Feb-2012 13:58	18-Feb-2012 10:22	-41.35	92.18	1060	$\beta\gamma$	10 B, 1 C
24	11682	23-Feb-2013 19:58	6-Mar-2013 06:34	-37.24	00.00	1135	$\beta\gamma$	5 B
25	11781	27-Jun-2013 20:10	5-Jul-2013 01:46	-11.43	82.70	859	$\beta\gamma$	4 B, 1 C
26	11946	4-Jan-2014 04:58	14-Jan-2014 05:34	-47.10	89.12	1196	$\beta\gamma$	3 C, 1 M
27	12003	9-Mar-2014 15:34	16-Mar-2014 22:10	-7.307	89.50	765	$\beta\gamma$	9 C
28	12271	24-Jan-2015 06:22	2-Feb-2015 14:22	-32.58	87.96	1087	$\beta\gamma$	1 B, 4 C
29	12339	4-May-2015 16:34	18-May-2015 17:58	-84.50	89.56	1636	$\beta\gamma$	3 B, 56 C, 3 M, 1 X
30	12543	7-May-2016 16:58	16-May-2016 17:58	-30.72	90.04	1043	$\beta\gamma$	7 B, 5 C
31	11079	8-Jun-2010 03:34	13-Jun-2010 13:46	12.102	89.36	589	$\beta\gamma$	1 B, 1 M
32	11326	20-Oct-2011 03:34	24-Oct-2011 15:46	23.325	86.04	534	$\beta\gamma$	
33	11385	22-Dec-2011 02:58	28-Dec-2011 22:22	-22.34	63.62	811	$\beta\gamma$	
34	11472	29-Apr-2012 04:10	8-May-2012 00:34	-51.84	60.73	915	$\beta\gamma$	
35	11807	28-Jul-2013 10:22	3-Aug-2013 12:58	-2.951	81.79	729	$\beta\gamma$	1 B
36	11081	11-Jun-2010 06:22	14-Jun-2010 23:22	35.170	90.15	439	$\beta\gamma$	6 B, 7 C, 1 M
37	11148	17-Jan-2011 01:58	21-Jan-2011 09:46	21.677	79.32	509	$\beta\gamma$	
38	11116	16-Oct-2010 19:22	19-Oct-2010 02:58	-2.952	30.11	259	$\beta\gamma$	
39	11510	18-Jun-2012 19:58	25-Jun-2012 04:22	-18.74	71.90	713	$\beta\gamma$	
40	11141	30-Dec-2010 21:34	6-Jan-2011 01:34	-1.415	81.40	736	β	10 B, 1 C
41	11072	20-May-2010 16:22	29-May-2010 12:34	-35.76	90.09	1050	β	4 B
42	11076	31-May-2010 04:10	7-Jun-2010 21:34	-16.68	89.09	925	β	1 B
43	11096	3-Aug-2010 12:46	14-Aug-2010 02:10	-63.10	74.95	1189	β	2 B
44	11132	3-Dec-2010 23:10	11-Dec-2010 10:22	-14.14	89.78	874	β	4 B
45	11143	6-Jan-2011 00:46	13-Jan-2011 12:46	-43.12	54.76	901	β	
46	11449	28-Mar-2012 09:10	3-Apr-2012 03:34	-3.404	78.27	680	β	
47	11551	20-Aug-2012 03:46	25-Aug-2012 16:58	-12.12	62.68	656	β	

Table 1 continued

Table 1 (continued)

Number	NOAA	Start Date	End Date	Start long. (Degrees)	End long. (Degrees)	Number of magnetograms	Hale class	Flare class
48	11843	17-Sep-2013 07:46	23-Sep-2013 01:58	-14.49	65.78	637	β	
49	11855	29-Sep-2013 18:10	7-Oct-2013 12:58	-32.89	78.70	896	β	
50	12119	18-Jul-2014 09:34	26-Jul-2014 04:46	-23.16	84.18	867	β	1 B
51	11152	2-Feb-2011 15:22	8-Feb-2011 08:46	-29.06	46.96	688	β	8 B
52	11630	6-Dec-2012 17:10	15-Dec-2012 08:22	-47.67	71.92	1028	β	11 B, 2 C
53	11211	8-May-2011 15:10	11-May-2011 15:22	3.4807	45.80	356	β	
54	11446	22-Mar-2012 16:58	27-Mar-2012 19:58	-17.52	52.96	570	β	2 B
55	11105	2-Sep-2010 02:10	8-Sep-2010 12:46	-0.349	92.62	772	β	13 B, 2 C
56	11130	27-Nov-2010 15:10	5-Dec-2010 12:22	-19.48	89.99	946	β	26 B, 1 C
57	11242	28-Jun-2011 02:10	5-Jul-2011 07:58	-9.091	90.76	860	β	7 B,
58	11300	17-Sep-2011 00:34	22-Sep-2011 10:58	17.306	93.13	594	β	
59	11460	15-Apr-2012 11:34	26-Apr-2012 13:22	-61.20	88.76	1290	β	2 B, 5 C

2. DATA AND ANALYSIS

2.1. Data

The Helioseismic and Magnetic Imager (HMI; Scherrer et al. 2012; Schou et al. 2012) onboard the Solar Dynamics Observatory (SDO; Pesnell et al. 2012) provides uninterrupted, full-disk, spectropolarimetric observations of the photosphere in the Fe I 6173 Å spectral line since 2010. The spectropolarimetric observations are inverted to provide the magnetic field vector at one level in the photosphere. This study utilizes the HMI Active Region Patches (HARP; Hoeksema et al. 2014), which are cutouts that track regions of interest (high-polarization regions such as active regions and plages) and contain, among others, maps of the three components of the magnetic field. The Cylindrical Equal Area (CEA) version of the definitive data is used, that is, cutouts for which the 180°-ambiguity has been resolved and the three components of the magnetic field vector B_r , B_p and B_t (equivalent to the three Cartesian components B_z , B_x and B_y) have been deprojected and remapped to the solar disk center.

A sample of 59 emerging active regions was studied, consisting of 20 β -, 24 $\beta\gamma$ - and 15 $\beta\gamma\delta$ -class regions (Table 1). These Hale classes were the peak complexity classes reached by the active regions while they traversed the Earth-facing solar disk. The magnetic complexity information was derived from the Space Weather Prediction Center (SWPC) of the National Oceanic and Atmospheric Administration (NOAA)¹. Information regarding the flaring activity of the regions was retrieved

from the standardized multivariate data set SWAN-SF (Angryk et al. 2020).

2.2. Derivation of non-neutralized electric currents

The method to derive the net electric currents is the one developed by Georgoulis et al. (2012) and is illustrated schematically in Figure 1a and 1b. The map of the vertical component of the magnetic field, B_r , is partitioned using a flux tessellation method (Barnes et al. 2005), with thresholds for B_r , minimum magnetic flux per partition and minimum partition size equal to 100 G, 5×10^{19} Mx and 40 pixels ($5.3 Mm^2$), correspondingly. For each partition, the total current is calculated via a surface integration of the electric current density, which is itself calculated using the differential form of Ampere’s law, rather than directly the integral form of Ampere’s law used by Georgoulis et al. (2012). The reason for this was to speed up the calculations. In Kontogiannis et al. (2017) it was shown that the difference between the two estimates were largely insignificant, in comparison to the accuracy of the magnetic field measurements. Then a baseline is needed to determine how much of the calculated electric current could be due to numerical effects and/or errors. First, the propagated error for the electric current δI is calculated using the corresponding errors δB_t and δB_p . The numerical effects are represented by the “current for the potential field” I_{pot} . This is done by calculating the vector of the current-free (potential) magnetic field via extrapolation (Alissandrakis 1981) and applying Ampere’s law on the potential magnetic field. The resulting electric current should be equal to zero but this is not the case due to numerical effects. Magnetic partitions are considered non-neutralized only if $I > 5 \times I_{pot}$ and $I > 3 \times \delta I$.

For each HARP cutout the method essentially produces a set of electric-current non-neutralized magnetic partitions, along with their corresponding net electric

¹ <https://www.swpc.noaa.gov/>

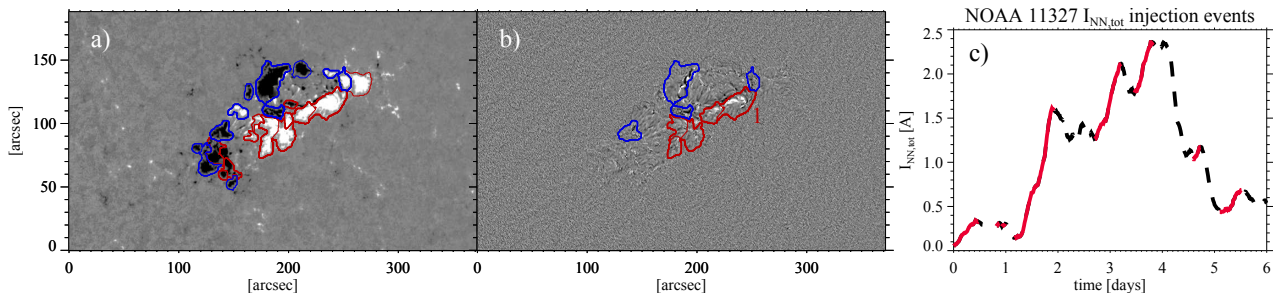


Figure 1. Illustration of the partitioning process, the calculation of the non-neutralized electric current, and the automated injection event detection method. a) Map of the B_r component for NOAA 11158, at 01:58 UT on 13 February 2011. The magnetic field values are clipped between ± 500 G to enhance visibility. The red (blue) contours indicate magnetic partitions with positive (negative) total electric current. b) Map of the vertical electric current density J_z , clipped between $\pm 7 \cdot 10^{-6}$ A cm $^{-2}$ to enhance visibility. The red (blue) contours indicate magnetic partitions with significant positive (negative) total electric current as per our selection criteria. The contour indicated with “1” is the partition with the maximum (in absolute value) non-neutralized electric current. c) Injection events (solid red) detected for the $I_{NN,tot}$ time series of NOAA 11327, up to $t = 6$ d.

currents I_{NN} . From this distribution, the total unsigned non-neutralized electric current $I_{NN,tot} = \sum |I_{NN}|$ and the maximum unsigned non-neutralized electric current $I_{NN,max} = \max(|I_{NN}|)$ of the cut-out can be calculated (Kontogiannis et al. 2017). For a series of HARP cutouts of a given active region, time series of $I_{NN,tot}$ and $I_{NN,max}$ were constructed, reflecting the evolution of the net electric currents in this region. Additionally, from the maps of the non-neutralized partitions the unsigned magnetic flux pertaining to those non-neutralized partitions $\Phi_{NN,tot}$ can be calculated.

Non-neutralized partitions are found along PILs (Georgoulis et al. 2012), but also during flux emergence events. These processes, i.e., emergence and PIL formation will be further discussed in Section 3, through a comparative analysis of $I_{NN,tot}$, $I_{NN,max}$, and Φ_{NN} time series, along with those of the total electric current I_z (namely, the surface integral of the electric current density J_z) and the total unsigned magnetic flux, Φ , provided by the Space Weather HARP data (SHARP; Bobra et al. 2014), for each HARP cut-out.

We note in passing that this method could potentially be used to study individual partitions, too, although we do not attempt this here. Tracking individual partitions should also account for potential merging or splitting effects (see e.g., Švanda et al. 2021). Instead, our focus in this work is to characterize active regions as a whole.

2.3. Automatic detection of injection events

An automated detection process was implemented to locate ascending branches of conspicuous peaks in $I_{NN,tot}$, which signify events of net electric current injection in the corresponding time series. To remove potential high frequency noise, the time series were smoothed with a running 6-hour window, corresponding to 31 points (as per the 12 minute cadence of the HMI vector

magnetograms). Then the local minima and maxima along with their positions were located. The injection events are segments of notable and persistent increase in $I_{NN,tot}$, and it is assumed that they are demarcated by a local maximum and the local minimum that precedes it. The residual high-frequency small-amplitude variability can cause the detection of several consecutive, short segments along one injection event. A proximity criterion was implemented to merge consecutive segments, i.e., for which the beginning of the following segment is found less than 1 hour after the end of the preceding. To avoid the merging of segments along decreasing parts of the time series, we demanded that the following segment had a higher average $I_{NN,tot}$ than the preceding. Finally, to avoid variations within the error margin, segments resulting in an increase of less than 10% were discarded. An example is illustrated in Figure 1c, for active region NOAA 11327. As per the imposed criteria, fairly isolated conspicuous events are always detected but consecutive weak events could be missed because they could be merged leading either to decreasing or marginal, within the error, trend. This could produce a slight underestimation of weak events, which does not, however, alter the conclusions of our study.

For the detected time series segments we determined the duration and the average injection rate using a linear fit. For the same segments we calculated the corresponding rates of the total unsigned magnetic flux Φ and the total unsigned flux of the non-neutralized partitions Φ_{NN} .

3. RESULTS

3.1. Example cases

3.1.1. Example of a β -class active region: NOAA 11551

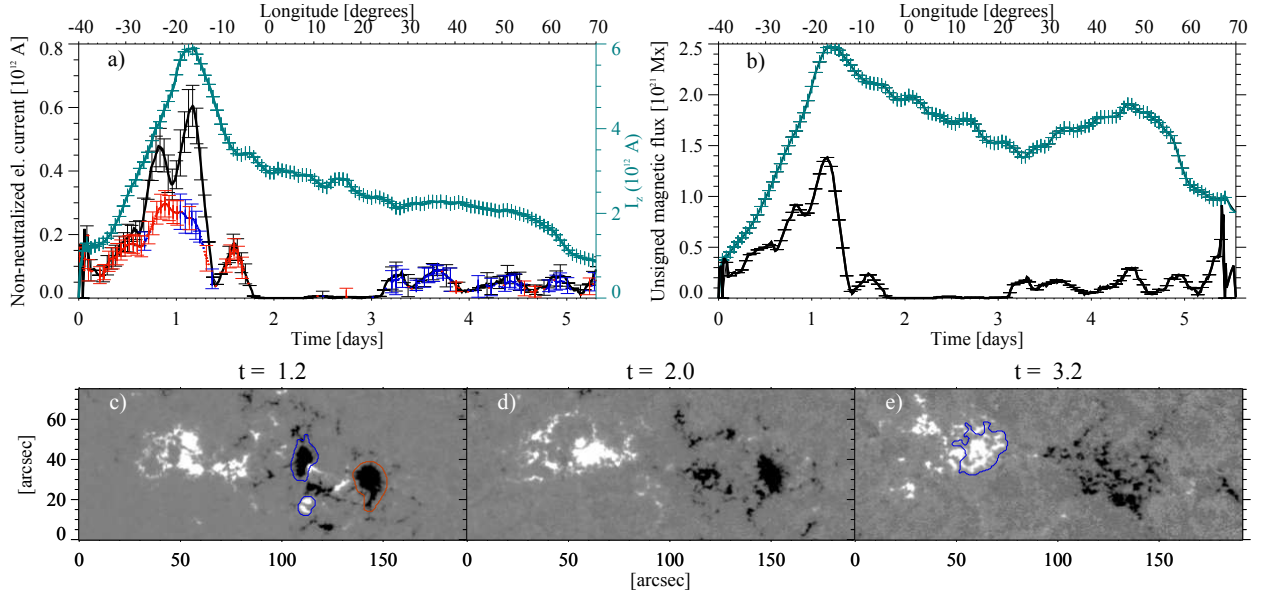


Figure 2. a) Time series of $I_{NN,tot}$ (black solid), $I_{NN,max}$ (blue for negative/red for positive) and I_z (petrol) for active region NOAA 11551. b) The total unsigned magnetic flux Φ (petrol solid) and the total unsigned magnetic flux of the non-neutralized partitions $\Phi_{NN,tot}$ (black). The upper x-axis denotes central meridian distance in both a and b. c-e) Maps of the vertical component B_r of the photospheric magnetic field at various instances. Blue and red contours indicate non-neutralized partitions carrying negative and positive electric current, correspondingly. The time is in decimal days since the first magnetogram of the series, taken on 20 August 2012, at 03:46 UT ($t = 0$).

Active region NOAA 11551 (Figure 2) started emerging on 20 August 2012, at 03:46 UT and evolved up to a β -type region. No flares were associated with the region during its passage along the Earth-facing solar hemisphere. Both I_z and Φ (petrol lines in panels (a) and (b), respectively) increased sharply within the first day of emergence and then started to decay. The decrease of I_z was sharp up to well into the second day, when the two polarities became fully separated and then it started decreasing slowly until the region decayed and rotated out of view. The magnetic flux exhibited an increase after the third day, during which the decrease of the electric current stagnated. After $t = 4.5$ d both the magnetic flux and the electric current decreased as the region moved past the 60° heliographic longitude. At such high central meridian distances the measurement of the magnetic field becomes less reliable due to projection and foreshortening effects, as well as the increased noise pattern appearing towards the limb (Hoeksema et al. 2014). The latter are known effects introducing an asymmetric bias in the values of the total unsigned magnetic flux, leading to higher, on average, values towards the western limb (see, e.g., Figure 6 of Kontogiannis et al. 2018).

The values of $I_{NN,tot}$ were around one order of magnitude lower than I_z (note the different y-axes in Figure 2a). Although the overall evolution of $I_{NN,tot}$, $I_{NN,max}$ and Φ_{NN} followed the general trend of the total

unsigned magnetic flux and unsigned total current, there were also notable differences. The total non-neutralized electric current (black line in Figure 2a) also increased during the first day, but exhibited a richer structure. The initial increase was followed by two sharp peaks, reaching up to 5×10^{11} and 6×10^{11} A, as well as a lower one seen during the decay. During the most pronounced peaks, $I_{NN,max}$ was always significantly lower than $I_{NN,tot}$ revealing the existence of more than one non-neutralized partitions (Kontogiannis et al. 2017), which developed during the first day, as the magnetic field emerged and opposite polarities started interacting. The sign of the $I_{NN,max}$ changed several times indicating that during the evolution of the region different non-neutralized partitions, with alternating signs of electric current, were taking the lead. The photospheric magnetogram in Figure 2c shows three non-neutralized partitions of neighboring opposite polarity magnetic flux. During the third day, when $I_{NN,tot}$ dropped to almost zero, the polarities were well separated (Figure 2d). After the end of the third day, $I_{NN,tot}$ and $I_{NN,max}$ increased again, similarly to I_z , exhibiting a series of peaks which reached up to 10^{11} A, until the region rotated out of view. At all times the Φ_{NN} followed closely $I_{NN,tot}$; despite being strongly correlated (Pearson correlation at 0.95), the two time series were not identical as seen e.g., by the different relative size of the two peaks around the end of the first day.

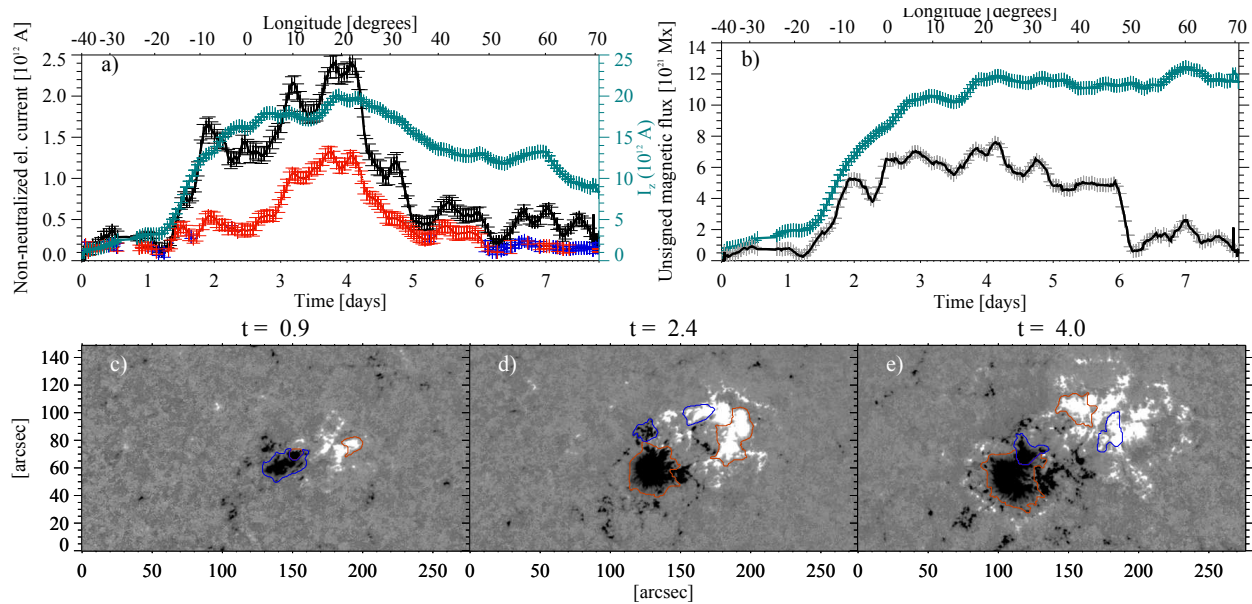


Figure 3. Same as Figure 2 for active region NOAA 11327. The first magnetogram of the series was taken on 18 October 2011, at 23:58 UT ($t = 0$).

3.1.2. Example of a $\beta\gamma$ -class active region: NOAA 11327

Active region NOAA 11327 (Figure 3) started emerging on 18 October 2011, at 23:58 UT, evolved up to a $\beta\gamma$ -type region, but produced no flares during its passage on the solar disk. The magnetic flux and the vertical electric current increased gradually during the first day of emergence and then increased precipitously during the following day reaching a maximum around the end of the fourth day. Then, I_z started to decrease slowly for as long as the region was observed, while Φ remained relatively constant, with a slight tendency to increase.

The $I_{NN,tot}$ was, overall, one order of magnitude lower than I_z and exhibited more structure, with discrete peaks and a more drastic decrease after the maximum at the end of the fourth day. There was a broad, low peak during the first day of emergence, when the two polarities were still close to each other, but $I_{NN,tot}$ decreased briefly as the dipole separated. It then increased sharply during the bulk of the emergence, during which more non-neutralized partitions appeared in close proximity (see also Figure 3d). In this case, however, the $I_{NN,max}$ did not change sign, which means that the corresponding non-neutralized partitions always carried positive electric current, as a result of one compact negative-flux, positive-current partition having formed (Figure 3d). Sign changes were observed after the end of the sixth day, when the net current in the active region had decreased considerably and the magnetic flux was scattered into several smaller partitions.

The total unsigned magnetic flux of the non-neutralized partitions, Φ_{NN} , followed a similar trend

as the $I_{NN,tot}$, with one notable difference: although $I_{NN,tot}$ exhibited sharp peaks at $t = 2, 3$ and 4 d, as well as a drastic decrease after the fourth day, the corresponding peaks in magnetic flux were not so pronounced and the overall variation of Φ_{NN} was relatively subtle until the end of the sixth day. This clearly implies that interaction between magnetic partitions can change the injected electric current significantly without notable changes in their magnetic flux.

3.1.3. Example of a $\beta\gamma\delta$ -class active region: NOAA 11158

Active region NOAA 11158 (Figure 4) started emerging on 10 February 2011, at 21:58 UT and developed into a $\beta\gamma\delta$ -type region. It produced the first X-class flare of Solar Cycle 24 and, having been closely monitored by the SDO, it was very well-studied (see, e.g., Tziotziou et al. 2013; Inoue et al. 2014; Vemareddy et al. 2015, and references therein).

During the first two days of evolution two bipoles emerged, a smaller one at the south-east (lower left) and a bigger one at the north-west (upper right). This led to a slow increase of the magnetic flux (Figure 4b), during most of which, there was also an increase in I_z and $I_{NN,tot}$ (Figure 4a). Initially, when the two polarities of each dipole started to separate, I_z remained almost constant, following closely the evolution of Φ , while $I_{NN,tot}$ decreased until the end of the second day. Avallone & Sun (2020) report a similar decrease in the degree of current neutralization. Our results suggest that the observed decrease of $I_{NN,tot}$ is a consequence of the separation of the dipoles.

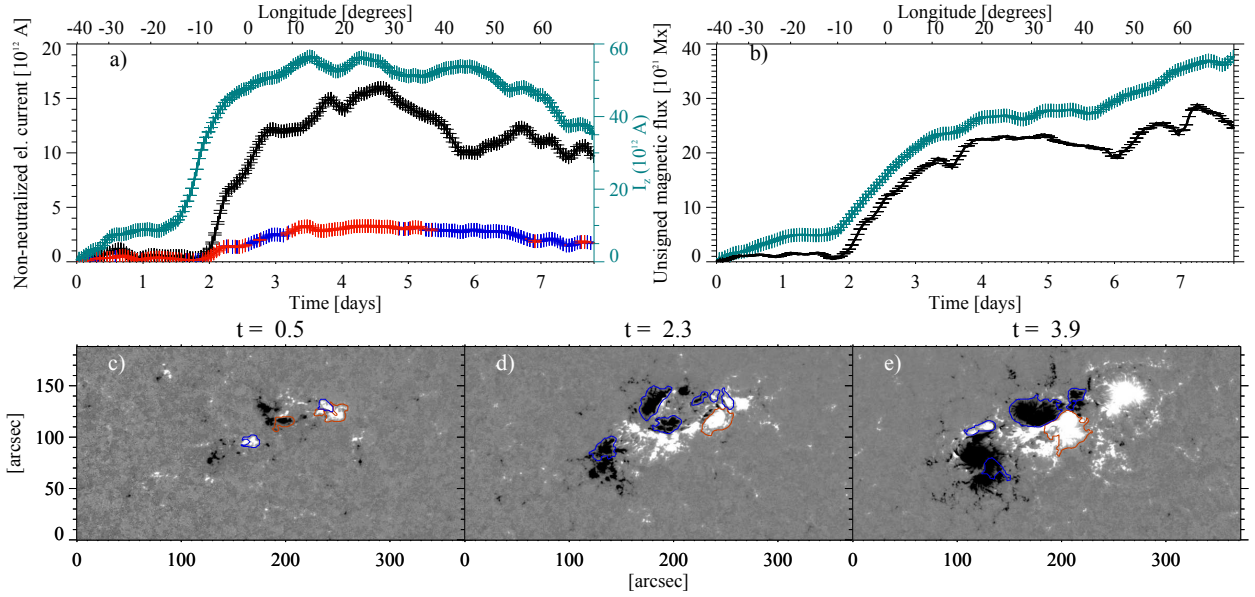


Figure 4. Same as Figure 2 but for active region NOAA 11158. The first magnetogram of the series was taken on 10 February 2011, at 21:58 UT ($t = 0$).

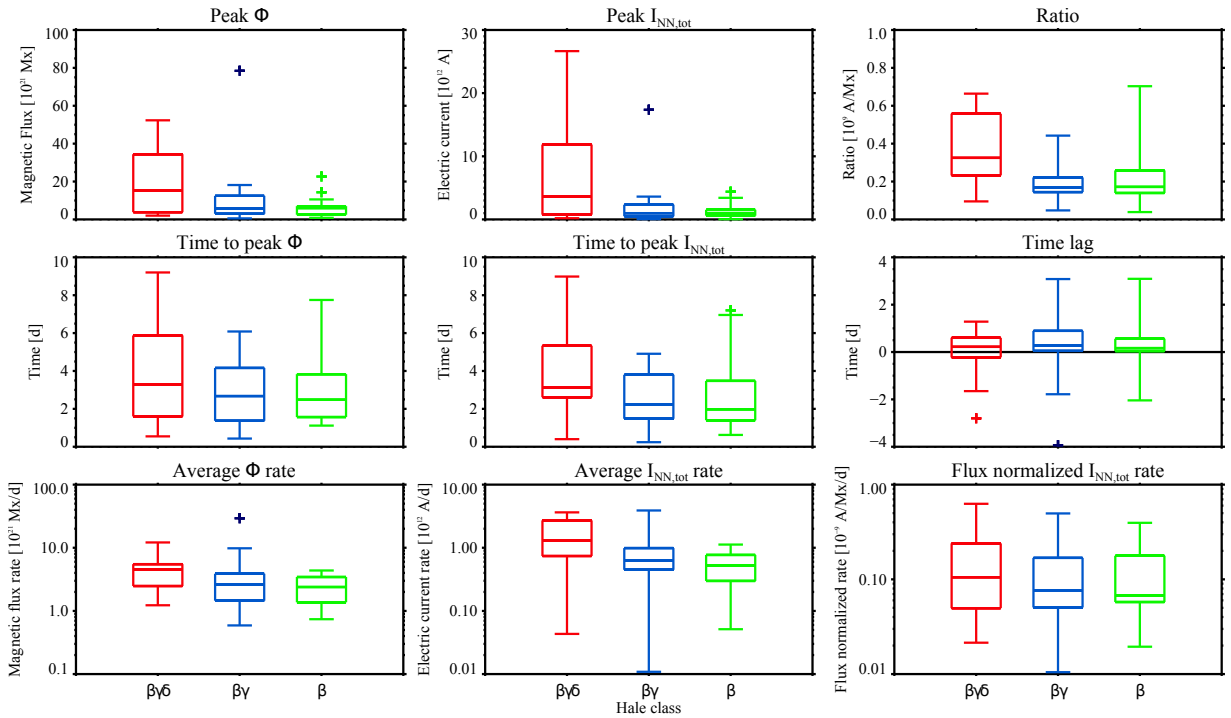


Figure 5. Box-and-whiskers plots of time series characteristics for the regions of Table 1. The lower and upper boundaries of the box indicate the 25th and 75th percentile, respectively, the horizontal line drawn inside the box indicates the median and the whiskers indicate the minimum and maximum value for each sample. All percentiles are calculated excluding outliers, which are found 3σ (the standard deviation of the sample) away from the median and are marked with crosses. The top row contains the peak values of Φ (left), $I_{NN,tot}$ (middle) and their ratio (right). The middle row contains the time when the corresponding peak values occurred (left and middle) as well as their time lag (right), with positive lag meaning that the peak in $I_{NN,tot}$ occurred first. The bottom row contains the average magnetic flux rate (left), the average $I_{NN,tot}$ rate (middle) and the flux-normalized average $I_{NN,tot}$ rate. Green, blue and red indicate β -, $\beta\gamma$ - and $\beta\gamma\delta$ -regions, respectively. All quantities were calculated for central meridian distances within $\pm 45^\circ$.

At the end of the second day the evolution of NOAA 11158 became dramatic, with massive emergence

of magnetic flux, accompanied by intense flaring activ-

ity, comprising several C- and M-class flares, as well as one X-class flare, at $t = 4.15$ d. The total unsigned flux increased almost twice as fast in comparison to the first two days, it reached a local maximum around $t = 3.4$ d and then increased with a much lower rate until $t = 5.3$ d. The flux further increased after $t = 6$ d. The increase of the electric current after the end of the second day was sharper, with both I_z and $I_{NN,tot}$ reaching local maxima at $t = 2.9$ d. Then the two parameters followed a slightly different evolution, I_z reaching a maximum at $t = 4$ d and $I_{NN,tot}$ reaching a maximum half a day later, at $t = 4.5$ d. As the active region evolved further and entered its decay phase, both parameters decreased slowly, with $I_{NN,tot}$ exhibiting a faster decrease. The $I_{NN,max}$ followed the increase of $I_{NN,tot}$, but reached a plateau after the end of the third day,

switching sign three times, as indicated by the different colors in Figure 4a. Since the flux was almost balanced during this phase (not shown) and the magnetic flux carried by the non-neutralized partitions, Φ_{NN} , also varied slowly (Figure 4b), this is interpreted as different magnetic partitions acquiring higher non-neutralized electric current as a result of their interaction. In NOAA 11158, $I_{NN,tot}$ is not an order of magnitude but only about 3-4 times lower than I_z , indicating that a significantly higher part of the region is carrying non-neutralized electric currents. Additionally, the $I_{NN,tot}$ is around five times higher than $I_{NN,max}$ indicating that many non-neutralized partitions along the PIL contribute to the total net current (see also Figure 3 in Kontogiannis et al. 2017). Strongly sheared and complicated PILs are typical characteristics of δ -spot regions, denoting a current-carrying magnetic structure in the regions' core.

Table 2. Table 2. Median values of the time series properties presented in Figure 5.

Hale Class	Peak Φ	Peak $I_{NN,tot}$	Peak $I_{NN,tot}/\Phi$	Peak time Φ	Peak time $I_{NN,tot}$	Φ rate	$I_{NN,tot}$ rate
	$10^{21} Mx$	$10^{12} A$	$10^9 AMx^{-1}$	days	days	$10^{21} Mxd^{-1}$	$10^{12} Ad^{-1}$
β	6.0	1.0	0.17	2.5	2.0	2.4	0.5
$\beta\gamma$	5.9	1.0	0.17	2.7	2.2	2.6	0.6
$\beta\gamma\delta$	15.4	3.6	0.3	3.3	3.1	4.5	1.3

3.2. Temporal behavior of non-neutralized electric currents

3.2.1. The temporal evolution of $I_{NN,tot}$

To generalize the previous discussion on the full sample of active regions contained in Table 1, we calculated some synoptic characteristics of the time series, such as the peak values of Φ and $I_{NN,tot}$, their occurrence times, as well as the corresponding average time lags between the peaks. These are given in decimal days from the start of the emergence and provide a measure of how fast the regions evolve up to their maximum magnetic flux and electric current. Dividing the peak values by the occurrence times, rudimentary Φ and $I_{NN,tot}$ variation rates were calculated. Figure 5 and Table 2 summarize these results.

The different magnetic complexity of active region classes β , $\beta\gamma$ and $\beta\gamma\delta$ is reflected in their total unsigned magnetic flux and electric current. As seen in the upper row of Figure 5, δ -regions clearly stand out in terms of maximum Φ and $I_{NN,tot}$, with median values being more than three times higher than the median $I_{NN,tot}$ values for β and $\beta\gamma$ -regions. We note in passing that the four,

non-outlier δ -spot regions with the lowest magnetic flux and non-neutralized electric current, found in the typical range for β -regions, produced none (NOAA 11561, 11431 and 11273) or only two C-class flares (NOAA 11645). From the $\beta\gamma$ -regions (Figure 5, upper row, blue boxes), the outlier is NOAA 12339, which in terms of flare productivity is truly comparable to δ -regions, having produced many C- and M- as well as one X-class flare. Similarly, the two outliers from the β -regions, namely NOAA 11130 and 11460, were also the most flare-prolific β -regions of the sample. These findings agree with the results of Kontogiannis et al. (2017), where a correlation was found between the flare index (Abramenko 2005) and the $I_{NN,tot}$, for a limited sample of regions. In fact the Pearson correlation coefficient between the peak $I_{NN,tot}$, $I_{NN,max}$ and the flare index for our sample is 0.82 and 0.87. A more thorough investigation on the connection with imminent eruptive activity is planned for the future.

The ratio of the peak $I_{NN,tot}$ over the peak Φ for δ -spot regions is almost twice as high as that of the rest of the sample. This is strong indication that the excess net current in these regions is not due to their larger size but due to their complexity. One may not completely rule out the ‘‘big region syndrome’’ implying large values

of non-potentiality metrics in large active regions for extensive properties, albeit net currents are inherently intensive properties, relying on internal structure and complexity. It is also possible that these regions have intrinsically higher electric current upon emergence.

The middle row of Figure 5 shows the absolute and relative timing of the Φ and $I_{NN,tot}$ peak values, that is, the time it takes for active regions to reach their maximum extent and net current content. For δ -spot regions, these times are longer, with NOAA 11515 and 12673 exhibiting the highest ones. These extreme active regions evolved over many days, during which new flux emerged near already established flux systems (Louis et al. 2014; Verma 2018). From the β -regions sample, NOAA 11460 is an outlier in terms of peak $I_{NN,tot}$ time. Overall, the peak values in Φ and $I_{NN,tot}$ are not synchronized. In most cases this difference is in the order few hours and the time lags are predominantly positive, which means that the peak in $I_{NN,tot}$ occurs earlier than the one in Φ . In some cases, magnetic field interactions or flux emergence in later stages of evolution can lead to the peak $I_{NN,tot}$ value to occur later than the Φ peak. This is also the case for the two outliers, NOAA 11273 and 11510, a $\beta\gamma\delta$ and a $\beta\gamma$ region, respectively. Therefore, the intrinsic details of flux emergence and subsequent photospheric motions determine the relative timing of magnetic flux and non-neutralized electric current.

Although it takes longer for the δ -spot regions to reach their peak Φ and $I_{NN,tot}$ values, these are much higher than those measured for the other complexity classes. Hence, δ -spot regions exhibit the highest rates (Figure 5, bottom row). The median value for the magnetic flux rates (see Table 2) is within the range of previous results by Otsuji et al. (2011), Norton et al. (2017), and Kutsenko et al. (2019), if converted to Mxh^{-1} . The flare-prolific $\beta\gamma$ -region NOAA 12339 is an outlier also in terms of magnetic flux rate. The median rate of $I_{NN,tot}$ for δ regions is twice as high as the ones measured for β and $\beta\gamma$ ones. The flux-normalized increase rates of $I_{NN,tot}$ are still higher for the most complex regions, which indicates that net current rates are not directly proportional to the magnetic flux (and thus the size) of active regions.

3.2.2. The temporal evolution of $I_{NN,max}$

While the time series of $I_{NN,tot}$ show how the total amount of non-neutralized electric currents evolves, the corresponding time series of $I_{NN,max}$ show how the electric current carried by the most strongly non-neutralized partition at each instance changes over time. As different parts of the region emerge and evolve, the partition carrying $I_{NN,max}$ can change as well, as does the asso-

ciated magnetic flux $\Phi_{NN,max}$. This is why, as shown in the descriptions of Figures 2, 3 and 4, the sign of the $I_{NN,max}$ may change during its evolution. In Figure 6, the corresponding time series of the sample are quantified, similarly to the preceding analysis, in order to find differences between the different complexity classes.

As seen in the panels of the first row of Figure 6, δ -spot regions are associated with the highest $I_{NN,max}$ and $\Phi_{NN,max}$ values. This means that as these regions evolve, their individual partitions develop the highest electric currents in comparison to the simpler ones. The ratio of the highest individual electric current $I_{NN,max}$ over the corresponding magnetic flux $\Phi_{NN,max}$ is statistically higher as the complexity of the region increases (NOAA 11682 is an outlier). These panels show that for the most complex regions, the increase in the net current is not proportional to the increase in the corresponding flux carried by the magnetic partitions.

The panels at the bottom row of Figure 6 show the time required for the peak value of $I_{NN,max}$ and $\Phi_{NN,max}$ to develop in the examined sample of active regions. Similarly to what was demonstrated in Figure 5, δ -spot regions take longer to evolve in comparison to $\beta\gamma$ and β regions. However, here the distinction between the three classes in terms of the time-lag between the peak values in $I_{NN,max}$ and $\Phi_{NN,max}$ is clearer. Notably, active region NOAA 11460, a flare-prolific β -region is again an outlier, demonstrating longer $I_{NN,max}$ peak time and shorter time lag, as well as higher peak $\Phi_{NN,max}$. In fact, the majority of δ -spot regions exhibit negative lag, meaning that the peak value of $\Phi_{NN,max}$ occurred earlier. This is another, clear indication that the net electric current continues to increase in non-neutralized partitions after they have fully emerged and reached their peak magnetic flux.

3.3. The relation between $I_{NN,tot}$, $I_{NN,max}$ and I_z

The three active regions presented in Figures 2, 3 and 4 differ not only in the amount of non-neutralized electric currents they contained, but also in the ratio of this electric current over I_z . The same is also true for Φ_{NN} , *i.e.*, the magnetic flux associated with $I_{NN,tot}$. Given that these quantities are the corresponding parts of I_z and Φ that pertain to the non-neutralized current part of the regions, it could be surmised that the part of an active region that carries significant net currents increases with magnetic complexity, which is highest for NOAA 11158 and lowest for NOAA 11551. For these regions the corresponding ratios were even lower also when the two polarities were well separated and had increased when magnetic flux was emerging or when opposite polarities were in close proximity.

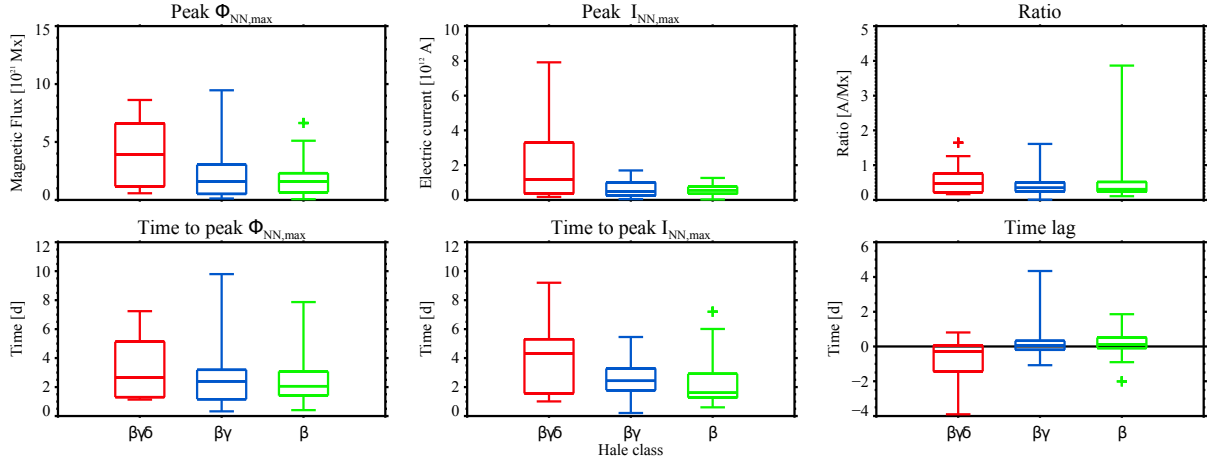


Figure 6. Same as Figure 5, but for the time series of $I_{NN,max}$ and the associated magnetic flux $\Phi_{NN,max}$. The top row contains the peak values of $\Phi_{NN,max}$ (left), $I_{NN,max}$ (middle) and their ratio (right). The bottom row contains the time when the corresponding peak values occurred (left and middle) as well as their time lag (right), with positive lag meaning that the peak in $I_{NN,max}$ occurred first. All the characteristics were calculated for central meridian distances lower than 45° EW.

Figure 7 extends these findings to the entire sample, showing the distribution of the non-neutralized portion of the regions, in terms of electric current and magnetic flux. These ratios were calculated at the times of maximum $I_{NN,tot}$, for the smoothed time series and for central meridian distances within $\pm 45^\circ$. As seen in the upper panel, δ -spot regions exhibit twice as high $I_{NN,tot}/I_z$ ratios compared to β and $\beta\gamma$ regions, the bulk of which are close to 0.1. The ratio Φ_{NN}/Φ exhibits smaller differences per complexity class, with a median around 0.65 for δ -spot regions. The higher ratios and smaller separation between the different classes could be a side effect of the calculation method, because the entire flux contained in a non-neutralized partition is considered non-neutralized although the net current may be occurring from a fraction of this partition (see, e.g., Fig 1c). Thus, magnetic flux associated with the current-carrying magnetic field could be overestimated. Nevertheless, δ -spot regions are located at the upper range of the Φ_{NN}/Φ ratio, while β and $\beta\gamma$ largely overlap each other. The ratio of non-neutralized electric current is not significantly correlated with the maximum magnetic flux of the region (Pearson correlation coefficient 0.2 for δ -regions). Therefore, the observed differences between different complexity classes do not reflect their total magnetic flux content.

Another interesting finding pertains to the ratio $I_{NN,tot}/I_{NN,max}$. For the bulk of β and $\beta\gamma$ regions it is less than 3, meaning that the $I_{NN,tot}$ is barely twice as high as $I_{NN,max}$, *i.e.*, the electric current carried by the most non-neutralized partition. Conversely, for δ regions the corresponding ratio acquires higher values, indicating the existence of many non-neutralized partitions in

close proximity, forming complicated PILs (Kontogiannis et al. 2017, 2019).

The ratio between the non-neutralized electric current over the current-carrying magnetic flux is examined at the bottom panel of Figure 7. No notable differences are seen for β - and $\beta\gamma$ -regions, but the current-carrying flux in δ -regions carries more electric current per unit non-neutralized flux in comparison to regions belonging to the other two classes. This result is in line with the observed highly-twisted structures (flux ropes and/or sheared magnetic arcades) these regions often host (see *e.g.*, Patsourakos et al. 2020, and references therein) and points to a systematic characteristic exhibited by these active regions.

3.4. Net electric-current injection events

As seen in Figures 2, 3 and 4, peaks in $I_{NN,tot}$ are found in sequence or superposition and indicate injection events and overall build-up of electric currents as a result of both emergence and photospheric interactions. To study these events in more detail, the detection algorithm was applied to the $I_{NN,tot}$ time series of the sample. The statistics for the detected events are summarized in Figure 8.

The relative frequency of the injection rates drops as the injection rate increases (Figure 8a), but the highest injection rates are found in δ -spot regions, followed by $\beta\gamma$ ones. The former show increased relative frequency of events with rates between 0.1 and $0.5 \cdot 10^{12} \text{ Ah}^{-1}$, whereas for β - regions they reach up to $0.25 \cdot 10^{12} \text{ Ah}^{-1}$. Overall the injection rate is moderately correlated with the event duration (0.45 Pearson correlation coefficient, Figure 8b). This correlation is slightly stronger for δ -regions (0.5) in comparison to the rest (0.38) and the

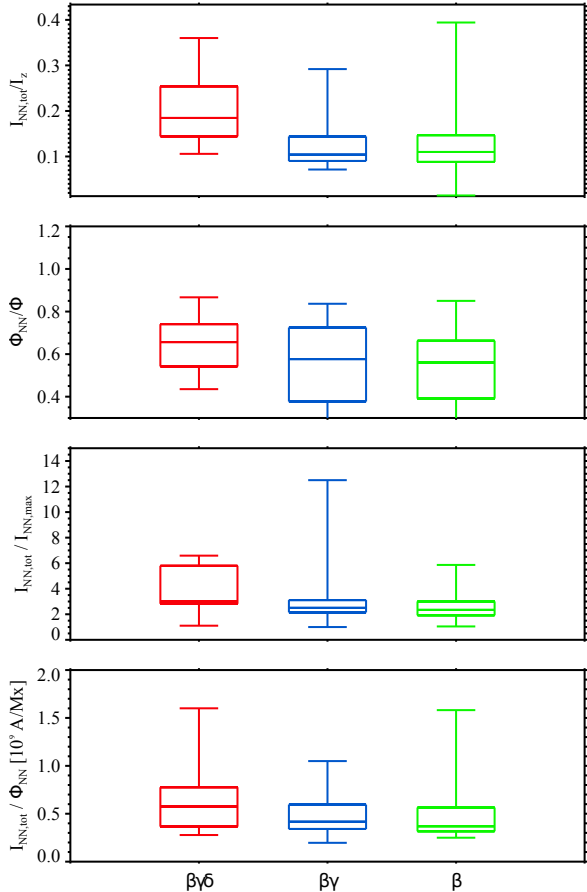


Figure 7. From top to bottom: box-and-whiskers plots of the ratios $I_{NN,tot}/I_z$, Φ_{NN}/Φ , $I_{NN,tot}/I_{NN,max}$, and $I_{NN,tot}/\Phi_{NN}$, calculated at the time of peak $I_{NN,tot}$.

duration of the events is longer for the most complex regions.

At the bottom row of Figure 8 the $I_{NN,tot}$ versus Φ (panel c) and Φ_{NN} (panel d) rates of the events are plotted. There is an overall positive correlation between these quantities (Pearson correlation coefficient equal to 0.54 and 0.52, respectively), reflecting the fact that in many cases the increase of the electric current is associated or happens during the emergence of magnetic flux. This is the case seen, e.g., in NOAA 11158 (Figure 4), during the first day and, mainly, during the third day, where the bulk of magnetic flux emerged and was accompanied by strong interaction between magnetic footpoints. However, the $I_{NN,tot}$ increase is not always associated with increasing magnetic flux since, as indicated by the two scatter plots, there is a considerable number of events associated with very small and even negative

magnetic flux rates, indicating flux decay. The correlation coefficients between $I_{NN,tot}$ and Φ rates for δ - $\beta\gamma$ - and β -regions are 0.66, 0.30 and 0.47. The corresponding correlation coefficient between the $I_{NN,tot}$ and Φ_{NN} rates (Figure 8d) are lower, that is, 0.52, 0.51 and 0.28. For the injection events with rates higher than $0.12 \cdot 10^{12} \text{ Ah}^{-1}$ (which are mostly events detected in δ -regions, see also Figure 8a) the correlation for δ -regions, which exhibit most of these rates, drops to 0.47 and 0.20 for Φ and Φ_{NN} , respectively. This correlation analysis for the injection events corroborates the conclusions drawn from the preceding analysis of time series properties. The current-carrying magnetic flux Φ_{NN} peaks earlier than the $I_{NN,tot}$, which keeps increasing (see Figure 6) and exhibiting injection events, even after Φ_{NN} is more or less constant (see *e.g.*, Figure 4).

4. DISCUSSION AND CONCLUSIONS

This study presents, to the best of our knowledge, the first statistical study of the evolution of non-neutralized electric currents in a statistically significant sample of solar active regions. For the derivation of non-neutralized electric currents the method of Georgoulis et al. (2012) was used, that relies on the calculation of the vertical electric current density and uses criteria on error propagation and numerical errors. The resulting time series of $I_{NN,tot}$ are relevant to the non-neutralized current-carrying part of an active region and exhibit a rich structure, not seen in the time series of the surface integrated total unsigned current, I_z . Through a comparative study of the $I_{NN,tot}$, $I_{NN,max}$, Φ_{NN} time series, along with those of I_z and Φ , we reach a number of conclusions regarding the evolution of net electric currents in active regions and the differences between regions of different magnetic complexity.

In all types of regions, the unsigned magnetic flux and the electric current exhibit similar (but far from identical) evolutionary trends, in terms of overall increase and decay. However, the peak values of Φ and $I_{NN,tot}$, representing their maximum size and complexity respectively, are in principle not synchronized, instead, the relative timing of these peaks depends not only on the emergence of magnetic flux but also on the subsequent interactions between magnetic partitions. Thus the build-up of net electric currents is a process driven by magnetic flux emergence but significantly shaped by interactions between flux systems. The latter factor is more pronounced in δ -spot regions, where $I_{NN,tot}$ continues to increase after the magnetic flux Φ_{NN} , associated with the net currents has peaked for most regions. The importance of polarity collision has been highlighted for some cases of δ regions that were extremely flare-prolific and

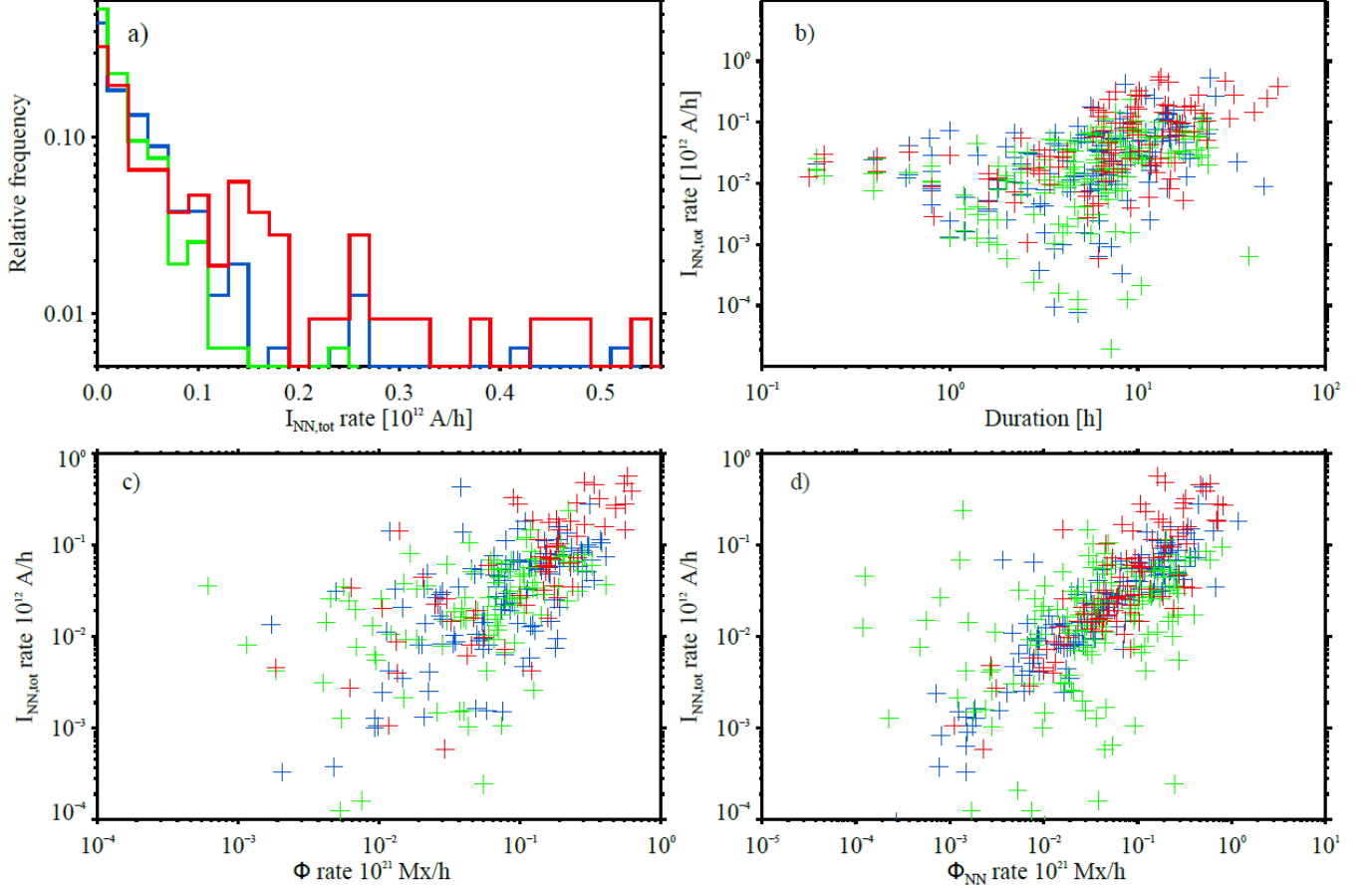


Figure 8. Electric-current injection event statistics for the active regions of Table 1. a) Histograms of injection rates, b) $I_{NN,tot}$ rate versus injection duration, c) $I_{NN,tot}$ rate vs. magnetic flux rate, and d) $I_{NN,tot}$ rate vs. magnetic flux rate of the non-neutralized partitions. In all panels, green, blue and red colors indicate statistics for β -, $\beta\gamma$ - and $\beta\gamma\delta$ -type regions, correspondingly.

exhibited various morphological configurations (Verma 2018; Toriumi et al. 2017; Chintzoglou et al. 2019). The results presented here generalize these case studies, from the point of view of net electric current injection.

During the flux decay phase, non-neutralized electric currents decrease faster than the magnetic flux, implying the vital relation between net electric currents and flux emergence along PILs, which leads to these currents' fast decrease during active region decay and their settling into more relaxed configurations with scattered, well-separated polarities. This decrease is more pronounced in $I_{NN,tot}$ than in I_z , corroborating the higher relevance of $I_{NN,tot}$ to magnetic complexity. Even during decay, though, incidental complexity due to interaction can still lead to injection of net electric currents into the corona, as indicated by significant peaks often seen in late stages of active region evolution.

To further study the injection of electric current in active regions, an automated detection method was implemented and a statistical study was carried out. The

more complex regions, i.e., $\beta\gamma$ and $\beta\gamma\delta$ were characterized by injection events with correspondingly higher rate and duration. The calculated correlations between the $I_{NN,tot}$ injection rates with those of Φ and Φ_{NN} reflect again the combined role of magnetic flux emergence and subsequent interactions in the formation of the three complexity classes. A future step would involve studying the characteristics of injection events on a larger sample of active regions, with no limitation on evolutionary stage, and explore the association with imminent flaring and eruptive activity. This might contribute clues toward prediction of flares and eruptions (i.e., CMEs), which is a key challenge in solar weather prediction (Kontogiannis 2023).

In this work, we extended the findings of Kontogiannis et al. (2017) regarding the relevance of non-neutralized electric currents to imminent flare productivity using a statistically significant sample of active regions. In several cases, $I_{NN,tot}$ evolution was unrelated to the size of active regions, in terms of their magnetic flux. Such “in-

tensive” behavior is considered highly relevant to CME prediction (Bobra & Ilonidis 2016). Our results indicate that the relevance of the examined parameters to flare and CME initiation is worth exploring in the future.

Regarding the relation between non-neutralized electric currents and complexity, it was shown that active regions with δ spots differ both in terms of peak values and evolution. They contain not only the highest magnetic flux but also the highest net electric currents, even when the latter are normalized to their peak magnetic flux content. The same is true for the increase rate of $I_{NN,tot}$, as well as the ratio $I_{NN,tot}/I_z$, *i.e.*, the part of the region that is current-carrying. For lower complexity cases, β -regions are practically indistinguishable from $\beta\gamma$ -regions in terms of those properties. Since the non-neutralized electric currents are directly associated with the presence of sheared PILs and, in our formulation, the ratio of $I_{NN,tot}$ over Φ or Φ_{NN} is a proxy of twist, the results presented here signify an inherently higher twist as well as different formation processes for the regions hosting δ -spots.

The study of Hale δ -class active regions in terms of net currents is extremely important both due to their high eruptive potential (Sammis et al. 2000) and because of our incomplete knowledge on which mechanism drives their formation (see *e.g.*, López Fuentes et al. 2003; Knizhnik et al. 2018, and references therein). The approach used in the present study can be used to distinguish and probe the net current-carrying part of an active region. Determining its properties can have implications on the formation mechanism, even more so since typical photospheric proxies that characterize active regions as a whole are not very efficient on distinguishing emerging flux tubes of different sub-photospheric properties (Knizhnik et al. 2018). In this context, Norton et al. (2022) found that the emergence rate of these regions is almost twice as high (1.9 times) as those of β , which is also corroborated by the present study (see Table 2). Here it was additionally shown that the non-neutralized electric currents of δ -spot regions increase 2.6 times faster than in other active region types, with individual injection events exhibiting even higher relative rates (Figure 8). The median of the maximum ratio Φ_{NN}/Φ was 0.65 (Figure 7), which is directly comparable with the so called “degree of δ ”, which Norton et al. (2022) defined as the magnetic flux fraction that partici-

pates in the δ configuration and amounts to 0.72 in their study. Recently, Levens et al. (2023) examined a limited sample of regions and showed that the current helicity, electric current and twist in magnetic knots, that is, the constituents of δ -spots, are all compatible with the kink instability. Therefore, we conclude that the approach used in the present study could be used in the future to contribute to the determination of δ -spots properties, providing more clues on the sub-surface condition in these regions.

An additional benefit of our methodology is that the derivation of $I_{NN,tot}$ is not based on assumptions concerning the chirality of the active region (as *e.g.*, in Avalone & Sun 2020) and/or specific region selection (Liu et al. 2017, 2024), which are required to determine the so-called degree of current neutralization (Török et al. 2014). The presented results are in line with those derived from the study of the degree of current neutralization (Liu et al. 2017; Vemareddy 2019; Avallone & Sun 2020; Liu et al. 2024; Barczynski et al. 2020; Wang et al. 2023; He et al. 2020). Another future step would be a comparative analysis of the evolution of active regions using both approaches, namely the degree of current neutralization along with the ratio $I_{NN,tot}/I_z$ (or its complement $1 - I_{NN,tot}/I_z$) and the neutrality factor proposed by Georgoulis et al. (2012).

We would like to thank the anonymous referee for providing useful comments, which improved the content and presentation of this study. This work was supported by grant KO 6283/2-1 of the Deutsche Forschungsgemeinschaft (DFG). For this paper, data from SDO/AIA and SDO/HMI were used. These are courtesy of NASA/SDO and the AIA, EVE, and HMI science teams and are publicly available through the Joint Science Operations Center at the jsoc.stanford.edu. Some of the calculations were performed using source codes made publicly available by the H2020 project FLARECAST (<https://dev.flarecast.eu/stash/projects/>).

Facilities: SDO

Software: SolarSoft IDL (Bentley & Freeland 1998; Freeland & Handy 1998), FLARECAST (Georgoulis et al. 2021)

REFERENCES

- Abramenko, V. I. 2005, ApJ, 629, 1141, doi: [10.1086/431732](https://doi.org/10.1086/431732)
- Alfvén, H., & Carlqvist, P. 1967, SoPh, 1, 220, doi: [10.1007/BF00150857](https://doi.org/10.1007/BF00150857)
- Alissandrakis, C. E. 1981, A&A, 100, 197
- Angryk, R. A., Martens, P. C., Aydin, B., et al. 2020, Scientific Data, 7, 227, doi: [10.1038/s41597-020-0548-x](https://doi.org/10.1038/s41597-020-0548-x)

- Aulanier, G., Démoulin, P., Schrijver, C. J., et al. 2013, *A&A*, 549, A66, doi: [10.1051/0004-6361/201220406](https://doi.org/10.1051/0004-6361/201220406)
- Aulanier, G., Janvier, M., & Schmieder, B. 2012, *A&A*, 543, A110, doi: [10.1051/0004-6361/201219311](https://doi.org/10.1051/0004-6361/201219311)
- Avallone, E. A., & Sun, X. 2020, *ApJ*, 893, 123, doi: [10.3847/1538-4357/ab7afa](https://doi.org/10.3847/1538-4357/ab7afa)
- Barczynski, K., Aulanier, G., Janvier, M., Schmieder, B., & Masson, S. 2020, *ApJ*, 895, 18, doi: [10.3847/1538-4357/ab893d](https://doi.org/10.3847/1538-4357/ab893d)
- Barnes, G., Longcope, D. W., & Leka, K. D. 2005, *ApJ*, 629, 561, doi: [10.1086/431175](https://doi.org/10.1086/431175)
- Bentley, R. D., & Freeland, S. L. 1998, in *ESA Special Publication, Vol. 417, Crossroads for European Solar and Heliospheric Physics. Recent Achievements and Future Mission Possibilities*, 225–228
- Bobra, M. G., & Ilonidis, S. 2016, *ApJ*, 821, 127, doi: [10.3847/0004-637X/821/2/127](https://doi.org/10.3847/0004-637X/821/2/127)
- Bobra, M. G., Sun, X., Hoeksema, J. T., et al. 2014, *SoPh*, 289, 3549, doi: [10.1007/s11207-014-0529-3](https://doi.org/10.1007/s11207-014-0529-3)
- Chintzoglou, G., Zhang, J., Cheung, M. C. M., & Kazachenko, M. 2019, *ApJ*, 871, 67, doi: [10.3847/1538-4357/aaef30](https://doi.org/10.3847/1538-4357/aaef30)
- Dalmasse, K., Aulanier, G., Démoulin, P., et al. 2015, *ApJ*, 810, 17, doi: [10.1088/0004-637X/810/1/17](https://doi.org/10.1088/0004-637X/810/1/17)
- Freeland, S. L., & Handy, B. N. 1998, *SoPh*, 182, 497, doi: [10.1023/A:1005038224881](https://doi.org/10.1023/A:1005038224881)
- Georgoulis, M. K. 2018, in *Electric Currents in Geospace and Beyond*, ed. A. Keiling, O. Marghitu, & M. Wheatland, Vol. 235, 371–390, doi: [10.1002/9781119324522.ch22](https://doi.org/10.1002/9781119324522.ch22)
- Georgoulis, M. K., Nindos, A., & Zhang, H. 2019, *Philosophical Transactions of the Royal Society of London Series A*, 377, 20180094, doi: [10.1098/rsta.2018.0094](https://doi.org/10.1098/rsta.2018.0094)
- Georgoulis, M. K., Titov, V. S., & Mikić, Z. 2012, *ApJ*, 761, 61, doi: [DOI:10.1088/0004-637X/761/1/61](https://doi.org/10.1088/0004-637X/761/1/61)
- Georgoulis, M. K., Bloomfield, D. S., Piana, M., et al. 2021, *Journal of Space Weather and Space Climate*, 11, 39, doi: [10.1051/swsc/2021023](https://doi.org/10.1051/swsc/2021023)
- Hale, G. E., Ellerman, F., Nicholson, S. B., & Joy, A. H. 1919, *ApJ*, 49, 153, doi: [10.1086/142452](https://doi.org/10.1086/142452)
- He, Y., Liu, R., Liu, L., et al. 2020, *ApJ*, 900, 38, doi: [10.3847/1538-4357/aba52a](https://doi.org/10.3847/1538-4357/aba52a)
- Hoeksema, J. T., Liu, Y., Hayashi, K., et al. 2014, *SoPh*, 289, 3483, doi: [10.1007/s11207-014-0516-8](https://doi.org/10.1007/s11207-014-0516-8)
- Inoue, S., Hayashi, K., Magara, T., Choe, G. S., & Park, Y. D. 2014, *ApJ*, 788, 182, doi: [10.1088/0004-637X/788/2/182](https://doi.org/10.1088/0004-637X/788/2/182)
- Jaeggli, S. A., & Norton, A. A. 2016, *ApJL*, 820, L11, doi: [10.3847/2041-8205/820/1/L11](https://doi.org/10.3847/2041-8205/820/1/L11)
- Janvier, M., Aulanier, G., Bommier, V., et al. 2014, *ApJ*, 788, 60, doi: [10.1088/0004-637X/788/1/60](https://doi.org/10.1088/0004-637X/788/1/60)
- Janvier, M., Aulanier, G., Pariat, E., & Démoulin, P. 2013, *A&A*, 555, A77, doi: [10.1051/0004-6361/201321164](https://doi.org/10.1051/0004-6361/201321164)
- Kazachenko, M. D., Lynch, B. J., Savcheva, A., Sun, X., & Welsch, B. T. 2022, *ApJ*, 926, 56, doi: [10.3847/1538-4357/ac3af3](https://doi.org/10.3847/1538-4357/ac3af3)
- Knizhnik, K. J., Linton, M. G., & DeVore, C. R. 2018, *ApJ*, 864, 89, doi: [10.3847/1538-4357/aad68c](https://doi.org/10.3847/1538-4357/aad68c)
- Kontogiannis, I. 2023, *Advances in Space Research*, 71, 2017, doi: [10.1016/j.asr.2022.10.008](https://doi.org/10.1016/j.asr.2022.10.008)
- Kontogiannis, I., Georgoulis, M. K., Guerra, J. A., Park, S.-H., & Bloomfield, D. S. 2019, *SoPh*, 294, 130, doi: [DOI:10.1007/s11207-019-1523-6](https://doi.org/10.1007/s11207-019-1523-6)
- Kontogiannis, I., Georgoulis, M. K., Park, S.-H., & Guerra, J. A. 2017, *SoPh*, 292, 159, doi: [DOI:10.1007/s11207-017-1185-1](https://doi.org/10.1007/s11207-017-1185-1)
- . 2018, *SoPh*, 293, 96, doi: [DOI:10.1007/s11207-018-1317-2](https://doi.org/10.1007/s11207-018-1317-2)
- Künzel, H. 1965, *Astronomische Nachrichten*, 288, 177
- Kutsenko, A. S., Abramenko, V. I., & Pevtsov, A. A. 2019, *MNRAS*, 484, 4393, doi: [10.1093/mnras/stz308](https://doi.org/10.1093/mnras/stz308)
- Leka, K. D., Canfield, R. C., McClymont, A. N., & van Driel-Gesztelyi, L. 1996, *ApJ*, 462, 547, doi: [10.1086/177171](https://doi.org/10.1086/177171)
- Levens, P. J., Norton, A. A., Linton, M. G., Knizhnik, K. J., & Liu, Y. 2023, *ApJL*, 954, L20, doi: [10.3847/2041-8213/acf0c6](https://doi.org/10.3847/2041-8213/acf0c6)
- Liu, Y., Sun, X., Török, T., Titov, V. S., & Leake, J. E. 2017, *ApJL*, 846, L6, doi: [10.3847/2041-8213/aa861e](https://doi.org/10.3847/2041-8213/aa861e)
- Liu, Y., Török, T., Titov, V. S., et al. 2024, *ApJ*, 961, 148, doi: [10.3847/1538-4357/ad11da](https://doi.org/10.3847/1538-4357/ad11da)
- Longcope, D. W., & Welsch, B. T. 2000, *ApJ*, 545, 1089, doi: [10.1086/317846](https://doi.org/10.1086/317846)
- López Fuentes, M. C., Démoulin, P., Mandrini, C. H., Pevtsov, A. A., & van Driel-Gesztelyi, L. 2003, *A&A*, 397, 305, doi: [10.1051/0004-6361:20021487](https://doi.org/10.1051/0004-6361:20021487)
- Louis, R. E., Puschmann, K. G., Kliem, B., Balthasar, H., & Denker, C. 2014, *A&A*, 562, A110, doi: [10.1051/0004-6361/201321106](https://doi.org/10.1051/0004-6361/201321106)
- McIntosh, P. S. 1990, *SoPh*, 125, 251, doi: [10.1007/BF00158405](https://doi.org/10.1007/BF00158405)
- Mitra, P. K., Joshi, B., & Prasad, A. 2020, *SoPh*, 295, 29, doi: [10.1007/s11207-020-1596-2](https://doi.org/10.1007/s11207-020-1596-2)
- Norton, A. A., Jones, E. H., Linton, M. G., & Leake, J. E. 2017, *ApJ*, 842, 3, doi: [10.3847/1538-4357/aa7052](https://doi.org/10.3847/1538-4357/aa7052)
- Norton, A. A., Levens, P. J., Knizhnik, K. J., Linton, M. G., & Liu, Y. 2022, *ApJ*, 938, 117, doi: [10.3847/1538-4357/ac8eb2](https://doi.org/10.3847/1538-4357/ac8eb2)

- Otsuji, K., Kitai, R., Ichimoto, K., & Shibata, K. 2011, PASJ, 63, 1047, doi: [10.1093/pasj/63.5.1047](https://doi.org/10.1093/pasj/63.5.1047)
- Parker, E. N. 1979, Cosmical magnetic fields: Their origin and their activity
- . 1996, ApJ, 471, 485, doi: [10.1086/177983](https://doi.org/10.1086/177983)
- Patsourakos, S., Vourlidas, A., Török, T., et al. 2020, SSRv, 216, 131, doi: [10.1007/s11214-020-00757-9](https://doi.org/10.1007/s11214-020-00757-9)
- Pesnell, W. D., Thompson, B. J., & Chamberlin, P. C. 2012, SoPh, 275, 3, doi: [10.1007/s11207-011-9841-3](https://doi.org/10.1007/s11207-011-9841-3)
- Sahu, S., Joshi, B., Prasad, A., & Cho, K.-S. 2023, ApJ, 943, 70, doi: [10.3847/1538-4357/acac2d](https://doi.org/10.3847/1538-4357/acac2d)
- Sammis, I., Tang, F., & Zirin, H. 2000, ApJ, 540, 583, doi: [10.1086/309303](https://doi.org/10.1086/309303)
- Scherrer, P. H., Schou, J., Bush, R. I., et al. 2012, SoPh, 275, 207, doi: [10.1007/s11207-011-9834-2](https://doi.org/10.1007/s11207-011-9834-2)
- Schou, J., Scherrer, P. H., Bush, R. I., et al. 2012, SoPh, 275, 229, doi: [10.1007/s11207-011-9842-2](https://doi.org/10.1007/s11207-011-9842-2)
- Semel, M., & Skumanich, A. 1998, A&A, 331, 383
- Severnyi, A. B. 1965, Soviet Ast., 9, 171
- Toriumi, S., Schrijver, C. J., Harra, L. K., Hudson, H., & Nagashima, K. 2017, ApJ, 834, 56, doi: [10.3847/1538-4357/834/1/56](https://doi.org/10.3847/1538-4357/834/1/56)
- Toriumi, S., & Wang, H. 2019, Living Reviews in Solar Physics, 16, 3, doi: [10.1007/s41116-019-0019-7](https://doi.org/10.1007/s41116-019-0019-7)
- Török, T., Leake, J. E., Titov, V. S., et al. 2014, ApJL, 782, L10, doi: [10.1088/2041-8205/782/1/L10](https://doi.org/10.1088/2041-8205/782/1/L10)
- Tsap, Y. T., Stepanov, A. V., & Kopylova, Y. G. 2022, ApJ, 939, 114, doi: [10.3847/1538-4357/ac9833](https://doi.org/10.3847/1538-4357/ac9833)
- Tziotziou, K., Georgoulis, M. K., & Liu, Y. 2013, ApJ, 772, 115, doi: [10.1088/0004-637X/772/2/115](https://doi.org/10.1088/0004-637X/772/2/115)
- van Driel-Gesztelyi, L., & Green, L. M. 2015, Living Reviews in Solar Physics, 12, 1, doi: [10.1007/lrsp-2015-1](https://doi.org/10.1007/lrsp-2015-1)
- Vemareddy, P. 2019, MNRAS, 486, 4936, doi: [10.1093/mnras/stz1020](https://doi.org/10.1093/mnras/stz1020)
- Vemareddy, P., Venkatakrisnan, P., & Karthikreddy, S. 2015, Research in Astronomy and Astrophysics, 15, 1547, doi: [10.1088/1674-4527/15/9/011](https://doi.org/10.1088/1674-4527/15/9/011)
- Venkatakrisnan, P., & Tiwari, S. K. 2009, ApJL, 706, L114, doi: [10.1088/0004-637X/706/1/L114](https://doi.org/10.1088/0004-637X/706/1/L114)
- Verma, M. 2018, A&A, 612, A101, doi: [10.1051/0004-6361/201732214](https://doi.org/10.1051/0004-6361/201732214)
- Švanda, M., Sobotka, M., Mravcová, L., & Výbošťoková, T. 2021, A&A, 647, A146, doi: [10.1051/0004-6361/202040127](https://doi.org/10.1051/0004-6361/202040127)
- Wang, W., Qiu, J., Liu, R., et al. 2023, ApJ, 943, 80, doi: [10.3847/1538-4357/aca6e1](https://doi.org/10.3847/1538-4357/aca6e1)
- Wheatland, M. S. 2000, ApJ, 532, 616, doi: [10.1086/308577](https://doi.org/10.1086/308577)
- Wilkinson, L. K., Emslie, A. G., & Gary, G. A. 1992, ApJL, 392, L39, doi: [10.1086/186420](https://doi.org/10.1086/186420)
- Zwaan, C. 1985, SoPh, 100, 397, doi: [10.1007/BF00158438](https://doi.org/10.1007/BF00158438)
- . 1987, ARA&A, 25, 83, doi: [10.1146/annurev.aa.25.090187.000503](https://doi.org/10.1146/annurev.aa.25.090187.000503)